Molecular dynamics simulations of shallow nitrogen and silicon implantation into diamond

Ossi Lehtinen,[1] Boris Naydenov,[2] Pia Börner,[1] Kristina Melentjevic,[2] Christoph Müller,[2] Liam Paul McGuinness,[2] Sebastien Pezzagna,[3] Jan Meijer,[3] Ute Kaiser,[1] and Fedor Jelezko[2]

[1]*Central Facility for Electron Microscopy, Group of Electron Microscopy of Materials Science, Ulm University, 89081 Ulm, Germany*

[2]*Institute for Quantum Optics, Ulm University, 89081 Ulm, Germany*

[3]*Institut für Experimentelle Physik II, Universität Leipzig, 04103 Leipzig, Germany*

(Received 15 October 2015; published 11 January 2016)

A solid understanding of the implantation process of N and Si ions into diamond is needed for the controlled creation of shallow color centers for quantum computing, simulation, and sensing applications. Here, molecular dynamics simulations of the shallow implantation of N and Si ions into diamond is simulated at 100–5000 eV kinetic energies and different angles of incidence. We find that ion channeling is an important effect with an onset energy depending on the crystal orientation. Consequently, the molecular dynamics simulations produce improved predictions as compared to standard Monte Carlo simulations. When implanting in a channeling direction, the spatial distribution of the channeled ions becomes markedly narrow, allowing a higher degree of control over the location of the nitrogen vacancy (NV^-) centers. A contamination layer on the ion entry surface reduces the fraction of channeled ions. A comparison to an experimentally determined depth profile based on a NMR signal from protons yields a quantitative agreement, validating the simulation approach.

DOI: 10.1103/PhysRevB.93.035202

I. INTRODUCTION

Color centers in diamond, with a nitrogen vacancy (NV^-) and silicon vacancy (SiV^-) as the most prominent examples, are one of the most promising systems for realizing solid-state qubits for quantum computing [1–3]. Further, an array of nuclear spins on the diamond surface, coupled to the color centers, can serve as a quantum simulator [4], and shallow NV^- are crucial for magnetic sensing applications [5], where single electron [6] and nuclear spin sensitivities [7–9] have been demonstrated.

A color center consists of a combination of an impurity atom (e.g., N or Si) at a substitutional position and a neighboring vacancy in the diamond lattice. Two alternative approaches have been employed for the creation of such structures. The first one is the introduction of impurities/vacancies through nitrogen [10–12] or silicon [13,14] ion implantation. The second one is by introducing an impurity gas during the diamond growth process [15–17]. The former approach provides the advantage of good spatial control over the location of the NV^- centers, limited by the precision of the implanter system and straggling of the ion (random deviations of the final ion position from the initial impact point due to random collisions with the target atoms).

The implantation approach can work in two ways [11]. First of all, if the target diamond has already an intrinsic concentration of, e.g., N, energetic particle bombardment can be used to introduce the vacancies required for the creation of color centers, with an annealing treatment allowing the vacancies to migrate and occasionally meet the impurity atoms to create the NV^- centers. Alternatively, a diamond of high purity can be implanted with the desired species to both introduce the impurities at a controllable depth and produce the vacancies for the color centers. The latter approach allows again a higher degree of control over the spatial distribution of the color centers, as the distribution of the impurities can also be controlled.

For all of the above mentioned applications, sub- to few-keV implantation is needed to limit the implantation depth of the color centers [5], and, indeed, near-surface NV^- centers have been generated by implanting N and N_2 at kinetic energies of 3–7 keV [11,12].

Computer simulations are often helpful for choosing the appropriate parametrization for the ion implantation process. The most commonly employed approach for modeling the implantation process is a Monte Carlo simulation, where the trajectory of the ions is followed in a randomized (essentially amorphous) medium, and statistics over the final positions, deposited energy per depth, etc., are gathered. The ubiquitous tool for running such simulations is the transport and range of ions in matter (TRIM) software package [18].

It is well known, however, that ion channeling, where the ions are guided along the crystallographic directions of the crystal, can have a strong influence on the trajectories of the ions [19]. Consequently, more sophisticated methods, such as molecular dynamics (MD) simulations, where the complete atomic structure of the target is accounted for, are required for properly modeling the implantation process into crystalline targets, especially in the keV range [20]. Indeed, MD simulations of N implantation into diamond at 4 keV kinetic energy in the [100] direction has been shown to exhibit strong channeling behavior [21]. MD has been successfully employed for describing the NV^--center implantation process also elsewhere [22] as well as for studying the structural transformations of diamond during ion irradiation [23].

In this paper, molecular dynamics simulations of the shallow implantation of N and Si into diamond are simulated at 100–5000 eV kinetic energies and different angles of incidence. Channeling is found to be an important effect in the process, with the exact onset energy depending on the crystal orientation, and consequently the molecular dynamics simulations produce improved predictions as compared to standard Monte Carlo simulations. When implanting in a channeling direction, the spatial distribution of the implanted ion becomes markedly narrow, allowing a higher degree of control over the location of the NV^- centers. When an adsorbate layer on top of the crystal is included in the simulations, the fraction

of the channeled ions becomes smaller. A comparison to an experimentally determined depth profile is made, and the depth distributions are found to quantitatively agree, although the experiment shows a broader distribution.

II. METHODS

The implantation process of N and Si atoms was simulated by analytical potential molecular dynamics, as implemented in the PARCAS code [19,24,25]. Here, the interactions of the atoms in the system are described by analytical potentials fitted to *ab initio* and/or empirical data, and the equations of motion of the atoms are numerically integrated to simulate the time evolution of the system. The C-C, C-N, and C-Si interactions were described by Tersoff type bond order potentials [26–28]. The short range interaction of the atoms, which is relevant in the case of high energy collisions of the atoms, was described by the Ziegler-Biersack-Littmark universal repulsive potential [18]. Such a simulation scheme has been earlier employed for the case of N and B implantation into graphene with density functional theory based sanity checks confirming the accuracy of the calculations [29].

For modeling the slowing down of the ions via electronic stopping when traversing the crystal, an ion energy dependent frictional force was applied as calculated by the Ziegler-Biersack-Littmark model [18]. In this case the energy is simply removed from the ion and does not contribute to damage production in the target [19]. The electronic stopping model employed here overestimates the electronic stopping power within the channels, however, as it is known that the electron density, and consequently the electronic stopping power, are reduced when traversing a channel [30]. An isotropic model was selected here for the sake of simplicity.

To differentiate between the target atoms and the incoming atom, we refer to the incoming atom as an "ion," although the charge of the ion was not taken into account, since the effects of low charge states are negligible in bulk materials. The simulation target was at 0 K before the impact. No temperature control was used in order to not influence the trajectory of the ion, at the possible cost of phonons crossing the periodic boundaries interacting with the created defects.

The simulated diamond target consisted of 15 000 atoms in a supercell of $\sim$18 nm $\times$ 18 nm $\times$ 266 nm, meaning the impacts were simulated into a relatively narrow rod of diamond, with periodic boundary conditions imposed over the long sides of the rod. The ions entered the system from the top of the rod, and the crystal was oriented to have the (100) plane as the entry surface. The two bottom atomic layers of the target were fixed to prevent drifting of the target after the impact. The narrow shape of the target was necessary for limiting the total number of atoms in the system, as approximately 20 000 simulation runs were required to gather enough statistics for the parameter space explored ($\sim$200 simulation runs for each parameter combination).

A simulation cell width of 10–15 Å was determined earlier to be large enough for evaluating ion distributions and primary damage [19]. Occasionally, collision cascades might reach the mirror image of itself over the periodic boundaries with such a setup, but these events are rare (see the Supplemental Material [31], Supplemental Fig. S1), and thus do not significantly influence the aggregate statistics over implantation distributions and damage profiles. To verify this, another set of simulations was run with a target of 40 Å $\times$ 40 Å $\times$ 148 Å and 40 656 atoms for selected parameter combinations, and no noticeable deviation from the earlier results was observed.

For gathering the statistics over the ion distributions, the final ion position was first corrected for any crossing events of the periodic boundaries. A vacancy was identified in the final atomic configuration if no atom was sitting within a radius of 0.4 Å from a lattice position. Equally, if a carbon atom was found more than 0.4 away from any lattice position, it was labeled as an interstitial. The cutoff value of 0.4 Å was determined empirically by conducting the analysis with different radii and finding a value range where the results do not significantly change. However, distances vary continuously in the data, so no "perfect" cutoff value could be determined. The depth distributions are plotted as kernel density estimates (KDEs) [32], that is, by superposing Gaussian kernels for each data point to produce a smoothed histogram. The width of the kernels was set to a value from 0.3 to 9 nm depending on the ion energy (setting a lower limit on the details visible in the final plots), and they were normalized to produce a density probability distribution per single ion impact.

The depth of shallow NV^- centers can be experimentally determined by measuring the magnetic field created by the fluctuations of protons on the diamond surface [7,16]. This method is very precise, but it is limited by the strength of the stochastic field, which is negligible at positions deeper than 10 nm. Thus the depth of the NV^- implanted with ion energies up to 5 keV can be estimated. An alternative method for determining the depth of vacancy centers using a scanning confocal microscope was recently published [33].

III. RESULTS AND DISCUSSION

The results of the simulations are summarized in Fig. 2 for nitrogen implantation and in Fig. 3 for silicon. For each energy-ion combination, three groups of graphs are plotted, i.e., the predicted ion ranges, and the vacancy and interstitial concentrations for each angle of incidence considered. For comparison, predictions from the TRIM software are included in the ion range plots. Although it is not possible to discuss every detail of the data here, some important aspects are highlighted in the following.

First, the solid red curves show the results for the normal angle of incidence (the [100] direction). For the two lowest energies, ions are implanted only very close to the surface, with a significant probability for reflection or backscattering (the integrated areas under the curve for 100 eV/200 eV are 0.76/0.95 for N and 0.41/0.95 for Si). Above these energies, practically all the ions penetrate the target, and are implanted at an increasing depth with increasing energy.

The influence of channeling becomes evident at 1000 eV for N and 2000 eV for Si as the range profile becomes broadened and a second shoulder appears to the right of the first peak, when some of the ions start penetrating much deeper into the target [21]. In the case of the lighter N, the second peak becomes higher than the first one, with a significant increase in

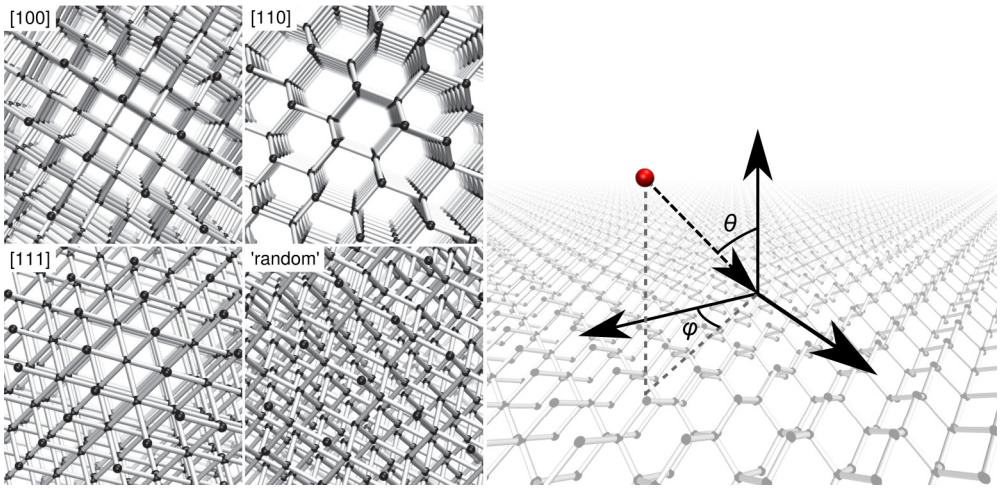

FIG. 1. Views through the diamond lattice in different directions in a ball-and-stick representation. The [100], [110], and [111] directions show open channels, through which energetic ions can easily pass. The "random" direction does not have straight unobstructed pathways through the lattice. The polar angle (θ) and azimuth (φ) defining the angle of incidence of the ion are shown on the right.

the projected range. The same effect, albeit less pronounced, can be observed in the case of Si.

Similar trends can be observed with the two other channeling directions ([110] and [111]), with differences in the onset energies for channeling. The [110] is an easy channeling direction due to the relatively large width of the channels (see Fig. 1), and channeling becomes important already at 200–500 eV. The ions also penetrate deeper than in the other cases. On the other hand, in the [111] direction the ions need to penetrate the close packed planes of the crystal, leading to a minimal channel width, and consequently a later onset energy and shorter ion ranges.

When the angle of incidence is tilted by 5° away from the [100] direction, the channeling effect is suppressed. However, the effect is still present with equal energy offsets as for the perfect [100] direction, meaning the ions are still directed in the channel despite the slightly off-axis direction. With the two other off-axis directions (tilted 15°/15° and 30°/30° away from [100]) and at all the simulated energies, the channeling effect disappears, and the projected ranges appear as single peaks slightly skewed towards the surface, typical of ranges in an amorphous target or for nonchanneling directions.

The final observation regarding the ion ranges is related to the TRIM simulations (calculated using a density of 3.5 g/cm^3 and the default displacement threshold of 28 eV for C, which does not influence the ion ranges). At low energies, the ions are systematically predicted to be implanted deeper by TRIM as compared to the MD simulations. This can be explained by the potential energy barrier the ions need to overcome at the surface of the target in the MD simulations. At higher energies (i.e., 2000 and 5000 eV) the TRIM results agree well with the simulations for the nonchanneling MD simulations (taking into account again the longer distance traveled by the ions in the case of tilted angles of incidence). However, in the case of channeling directions, the TRIM predictions deviate strongly from the MD results, which is an expected result, as the TRIM simulations do not take the crystal structure into account.

The radial straggling values for all simulated combinations of parameters are summarized in Table I. The values are determined as the root mean square of the deviations from the projected initial trajectory of the ion. Thus, if the implantation is conducted at a tilted angle, a wider distribution in the in-plane direction should be expected due to the mixing of the implantation range distribution and radial straggling.

Three features stand out from the straggling data. First of all, radial straggling increases with increasing ion energy in all cases, as expected. Second, N ions show consistently higher radial straggling than Si. Importantly, the straggling values are, in most of the cases, significantly lower in the channeling direction, as compared to the nonchanneling directions. This

TABLE I. Radial straggling in nm for each ion/energy/direction combination. The values are determined as the projected root mean square distance from the initial trajectory of the ion.

	[100]		[110]		[111]		5°/5°		15°/15°		30°/30°	
E (eV)	N	Si	N	Si	N	Si	N	Si	N	Si	N	Si
100	0.9	0.4	1.5	1.2	1.5	1.0	1.0	0.5	1.2	0.7	1.4	0.9
200	1.5	0.6	2.4	1.2	2.3	1.3	1.6	0.6	2.0	0.7	2.1	1.3
500	1.8	1.0	1.6	1.5	2.2	1.7	2.1	1.0	2.9	1.5	3.0	2.2
1000	4.0	1.6	2.5	1.5	5.0	3.1	3.6	2.1	5.0	2.4	5.9	3.1
2000	6.7	3.1	9.1	2.7	8.5	4.4	9.0	3.6	11.1	5.0	10.9	5.0
5000	13.2	5.8	7.0	5.2	18.1	7.0	20.2	9.0	28.5	10.9	27.7	13.5

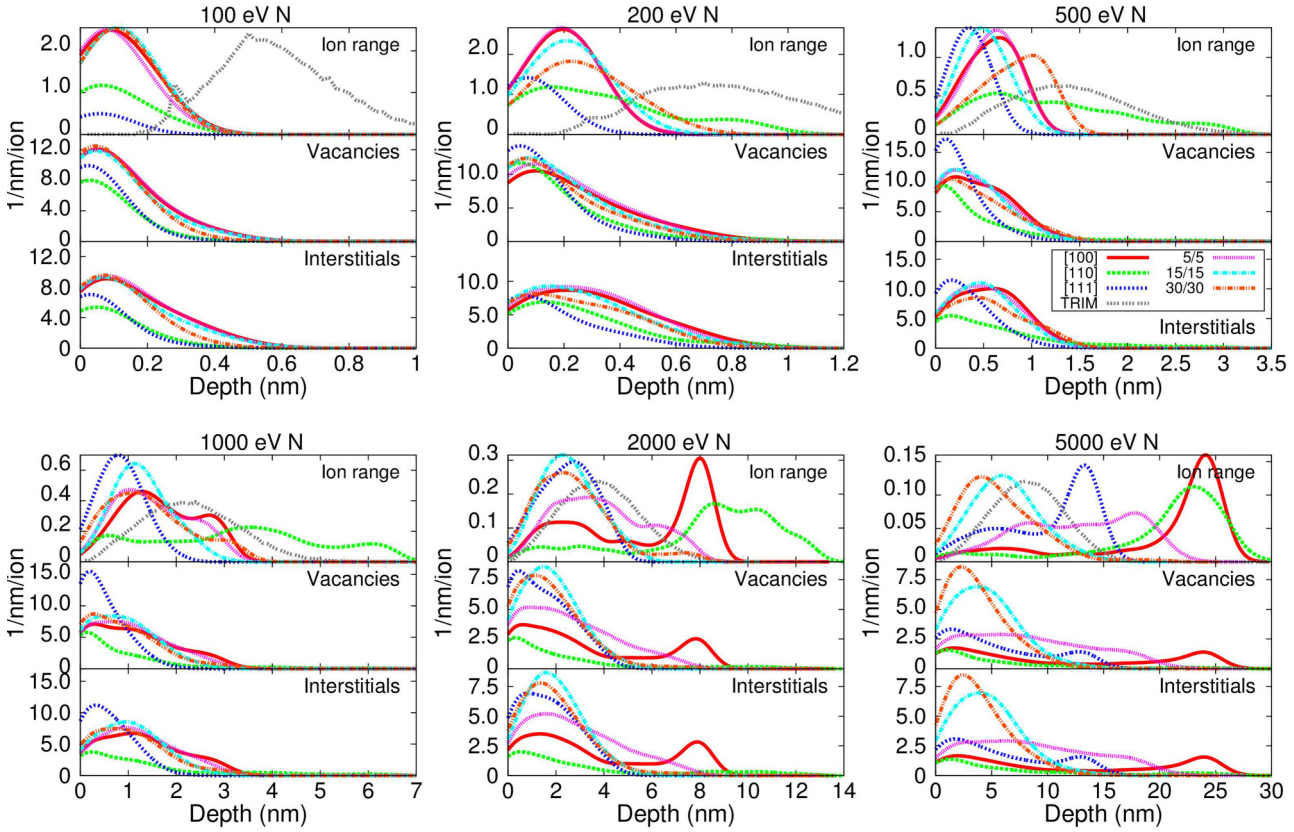

FIG. 2. Implantation of nitrogen into diamond. This set of graphs shows the predicted implantation depths, and the predicted vacancy and interstitial concentrations for six energies and six angles of incidence. The angles of incidence are selected as the three main crystal directions ([100], [110], and [111]) where channeling is expected and three nonchanneling directions, with the, e.g., 30/30, indicating the azimuth and the polar angle of the direction of incidence (see Fig. 1 for the definitions). All the values are normalized to give the predicted concentration per ion and per nm. Ion ranges, as predicted by the TRIM software, are displayed for each energy for comparison.

means more control over the final lateral position of the ions can be achieved when implanting in a channeling direction.

In addition to the implanted N or Si atoms, vacancies are needed for creating the NV^- and SiV^- centers. The middle graphs in Figs. 2 and 3 display the predicted vacancy distributions for each parametrization. At low energies and at nonchanneling directions, the vacancy distribution is a single peaked distribution with the maximum slightly closer to the surface than the ion range maximum. This is consistent with the Bragg peak description, where a maximum in the transferred energy is expected to be close to the end of the ion trajectories, as the nuclear scattering cross section increases with decreasing kinetic energy of the ion.

Again, at higher energies and at channeling directions, the picture changes. While traversing a channel, the ions scatter with atom columns instead of individual atoms, which leads to a relatively low energy transfer per target atom. Thus, damage production is strongly suppressed during a channeling event. However, a peak in the vacancy concentration close to the surface remains, since not all of the incident ions are channeled. These features are most prominent in the [110] direction. In the case of the N ion, [100] direction, and at energies of 2000 and 5000 eV, a second peak appears at the end of the trajectories, correlated with the peak in the ion ranges. With Si, such a clear second peak does not appear at any of the simulated energies. It is, however, possible that at higher kinetic energies also Si would display such features, based on the generally later onset of features as a function of energy with Si, as compared to N.

The interstitial distributions follow closely the vacancy distributions. With the employed definitions for interstitials and vacancies, the total numbers are identical (minus possible sputtered atoms). The kinetic energies of the displaced atoms at the ion energies used are relatively low, meaning they do not move far from the initial positions. Statistics on how far atoms are displaced can be found in the Supplemental Material [31], with Supplemental Fig. S1 showing that the displacements are predominantly in the range of a few Å. These results further justify the use of a narrow simulation cell.

As the sample surface is not necessarily atomically clean during the implantation, another set of simulations was run for the [100] direction, with a contamination layer included. The contamination was modeled by a sp^2-coordinated graphene flake placed at a randomized position on top of the target surface. The results are summarized in Fig. 4 and in the Supplemental Material [31], Supplemental Fig. S2. At low energies, the penetration probability was reduced. At higher energies, the general behavior was the same as with a clean surface, but the fraction of channeled ions was reduced. This effect is understandable, as the contamination atoms can scatter

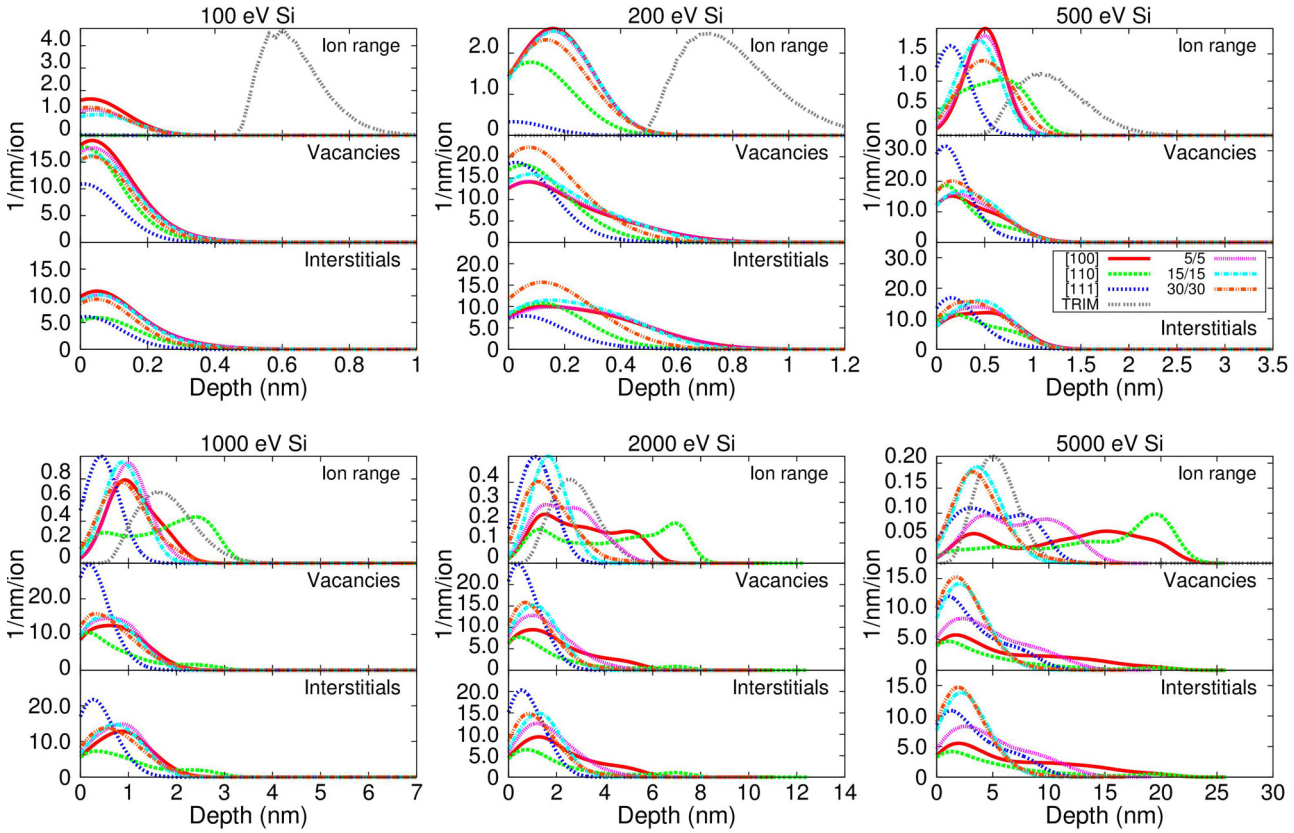

FIG. 3. Implantation of silicon into diamond. This set of graphs shows the predicted implantation depths, and the predicted vacancy and interstitial concentrations for six energies and six angles of incidence. The angles of incidence are selected as the three main crystal directions ([100], [110], and [111]) where channeling is expected and three nonchanneling directions, with the, e.g., 30/30, indicating the azimuth and the polar angle of the direction of incidence (see Fig. 1 for the definitions). All the values are normalized to give the predicted concentration per ion and per nm. Ion ranges, as predicted by the TRIM software, are displayed for each energy in the case of a normal angle of incidence for comparison.

the incoming ions, leading to deviations from the perfect channeling trajectories.

Finally, a comparison to experimentally determined implantation depths was made to verify the reliability of the simulation results. $^{15}N^{+}$ ions were implanted at a kinetic energy of 1600 eV in the normal direction of the (100) surface. The surface was cleaned by hydrogen plasma prior to the implantation, and the ion dose was kept low enough for identifying individual NV^{-} centers. After implantation, the diamond was annealed at 900 °C in vacuum, to enable formation of the NV^{-} centers. The measured depths of a total number of 29 NV^{-} centers are plotted in Fig. 5 as a KDE.

A set of 1400 MD simulations was run with identical parametrization and the results are also plotted in Fig. 5 along with a TRIM calculation for comparison. The experimental depth profile and the sharp peak produced by the channeled ions in the MD results are close to each other, while the TRIM prediction matches the experiment rather poorly. The experimental distribution is broader than the simulated distribution, but the position of the main peak is predicted with good accuracy. Interestingly, no NV^{-} centers are detected close to the surface, although the nonchanneled ions stop there, according to the MD results, which would imply that the channeled ions produce defect distributions more favorable to NV^{-}-center formation. Another possible explanation for the absence of the near-surface NV^{-} centers is charge neutralization close to the surface, which would render them undetectable.

Possible explanations for the broadening of the experimental profile are (a) the annealing treatment, as the implanted N atoms might diffuse at the elevated temperature, (b) residual contamination on the sample surface, e.g., a few molecule thick water layer, which was previously shown to influence the implantation depth profiles, and (c) deviations from the ideal [100] direction of the impinging ions, which also was shown earlier to lead to broadened features.

IV. CONCLUSIONS

To conclude, a large set of analytical potential MD simulations of 100–5000 eV N and Si implantation in diamond with different angles of incidence were run to predict the resulting implantation depths, and the vacancy and interstitial depth profiles. The role of ion channeling was found to be important, with the onset energy depending on the crystal orientation, and explicitly accounting for the crystal structure of the target is thus essential to correctly simulate the implantation process.

Implantation at channeling directions with energies in the keV range was observed to produce sharply peaked depth profiles in terms of implantation depth and vacancy/interstitial

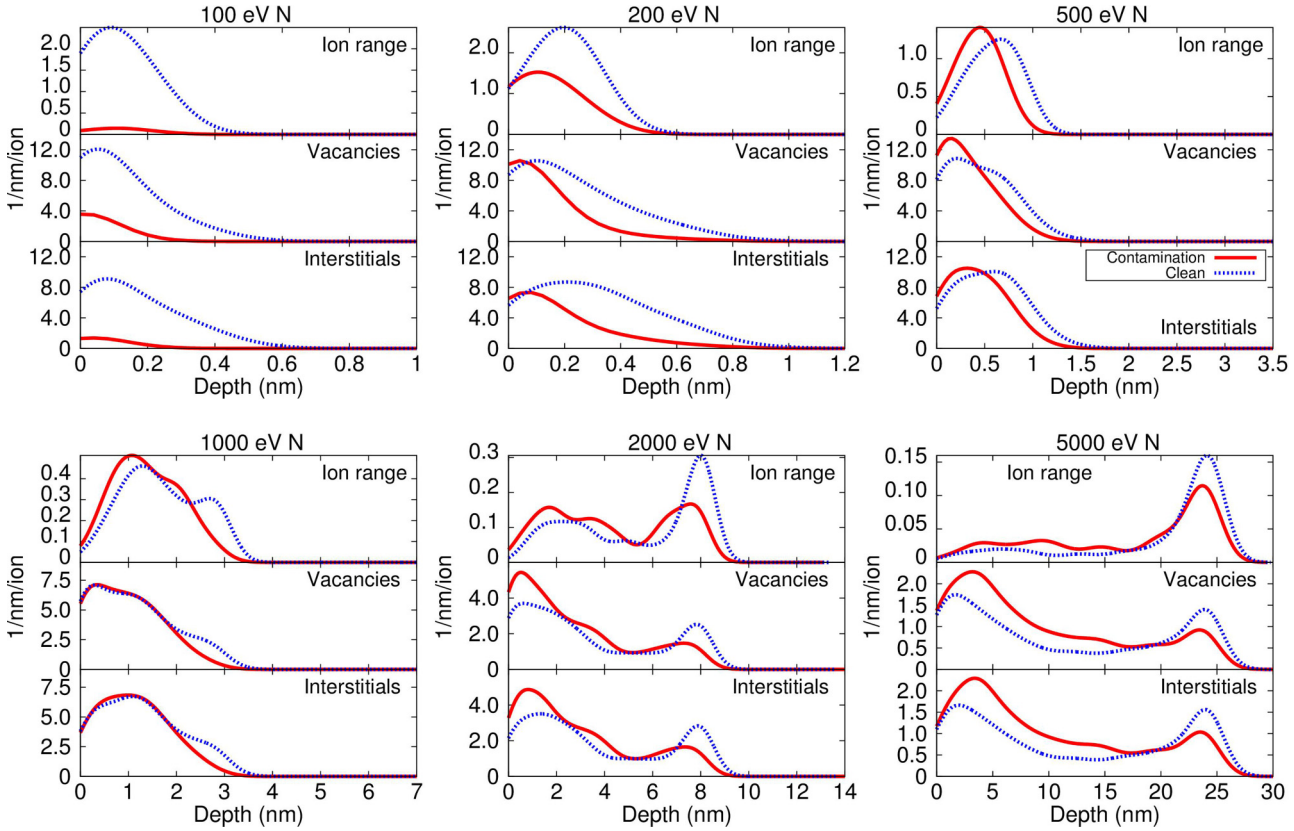

FIG. 4. Simulated depth profiles for N ions with and without a graphitic contamination layer. The simulations are for the [100] channeling direction. At low energies, ion penetration is suppressed by the contamination, while at higher energies the contamination leads to a reduction in the fraction of channeled ions. See the Supplemental Material [31], Supplemental Fig. S2, for results with Si ions.

production, which can be advantageous when precise control of the localization of the color centers is desired. A further advantage, when implanting in a channeling direction, is the reduction of radial straggling. On the other hand, if implantation very close to the surface, combined with high vacancy yields (requiring high ion energies), is desired, non-channeling directions can be advantageous. A contamination layer adsorbed on top of the crystal was found to reduce the fraction of the channeled ions.

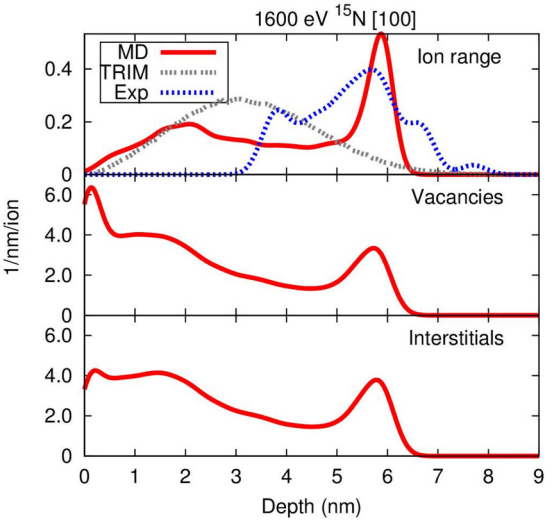

FIG. 5. A comparison between simulations and experiment. The red curves show the MD simulated implantation depth and the predicted vacancy and interstitial concentrations when implanting 1600 eV ^{15}N ions in the [100] direction. The blue dashed line shows the experimentally determined depth profile. The gray dashed line shows the depth profile as predicted by a TRIM simulation.

Furthermore, a comparison to an experimental data set on the implantation depth of 1600 eV $^{15}N^{+}$ ions implanted in the [100] direction resulted in a quantitative agreement between the depth ranges, confirming the validity of the simulation approach.

The data set presented here can be useful for the generation of shallow color centers in diamond. The inclusion of the crystal structure in the theoretical model results in more reliable predictions on the generated depth profiles as compared to standard Monte Carlo simulations. Based on the presented data, the best implantation parametrization, in terms of ion energy and angle of incidence, can be selected depending on the requirements of each application.

ACKNOWLEDGMENTS

This work was supported by the ERC Synergy grants BioQ and PoC, the EU (DIADEMS, EQUAM, SIQS), the DFG (SFB TRR/21), Volkswagenstiftung, and Bundesministerium für Bildung und Forschung (ARCHES award). B.N. is grateful to the Postdoc Network program of the IQST.

[1] M. W. Doherty, N. B. Manson, P. Delaney, F. Jelezko, J. Wrachtrup, and L. C. Hollenberg, Phys. Rep. **528**, 1 (2013).

[2] W. Pfaff, B. J. Hensen, H. Bernien, S. B. van Dam, M. S. Blok, T. H. Taminiau, M. J. Tiggelman, R. N. Schouten, M. Markham, D. J. Twitchen, and R. Hanson, Science **345**, 532 (2014).

[3] P. Neumann, N. Mizuochi, F. Rempp, P. Hemmer, H. Watanabe, S. Yamasaki, V. Jacques, T. Gaebel, F. Jelezko, and J. Wrachtrup, Science **320**, 1326 (2008).

[4] J. Cai, A. Retzker, F. Jelezko, and M. B. Plenio, Nat. Phys. **9**, 168 (2013).

[5] J. Wrachtrup, F. Jelezko, B. Grotz, and L. McGuinness, MRS Bull. **38**, 149 (2013).

[6] F. Shi, Q. Zhang, P. Wang, H. Sun, J. Wang, X. Rong, M. Chen, C. Ju, F. Reinhard, H. Chen, J. Wrachtrup, J. Wang, and J. Du, Science **347**, 1135 (2015).

[7] T. Staudacher, F. Shi, S. Pezzagna, J. Meijer, J. Du, C. A. Meriles, F. Reinhard, and J. Wrachtrup, Science **339**, 561 (2013).

[8] H. J. Mamin, M. Kim, M. H. Sherwood, C. T. Rettner, K. Ohno, D. D. Awschalom, and D. Rugar, Science **339**, 557 (2013).

[9] C. Müller, X. Kong, J.-M. Cai, K. Melentijevic, A. Stacey, M. Markham, D. Twitchen, J. Isoya, S. Pezzagna, J. Meijer, J. Du, M. Plenio, B. Naydenov, L. McGuinness, and F. Jelezko, Nat. Commun. **5**, 4703 (2014).

[10] J. Meijer, B. Burchard, M. Domhan, C. Wittmann, T. Gaebel, I. Popa, F. Jelezko, and J. Wrachtrup, Appl. Phys. Lett. **87**, 261909 (2005).

[11] J. R. Rabeau, P. Reichart, G. Tamanyan, D. N. Jamieson, S. Prawer, F. Jelezko, T. Gaebel, I. Popa, M. Domhan, and J. Wrachtrup, Appl. Phys. Lett. **88**, 023113 (2006).

[12] S. Pezzagna, B. Naydenov, F. Jelezko, J. Wrachtrup, and J. Meijer, New J. Phys. **12**, 065017 (2010).

[13] C. Wang, C. Kurtsiefer, H. Weinfurter, and B. Burchard, J. Phys. B **39**, 37 (2006).

[14] S. Tamura, G. Koike, A. Komatsubara, T. Teraji, S. Onoda, L. P. McGuinness, L. Rogers, B. Naydenov, E. Wu, L. Yan, F. Jelezko, T. Ohshima, J. Isoya, T. Shinada, and T. Tanii, Appl. Phys. Express **7**, 115201 (2014).

[15] K. Ohno, F. J. Heremans, L. C. Bassett, B. A. Myers, D. M. Toyli, A. C. Bleszynski-Jayich, C. J. Palmstrïm, and D. D. Awschalom, Appl. Phys. Lett. **101**, 082413 (2012).

[16] K. Ohashi, T. Rosskopf, H. Watanabe, M. Loretz, Y. Tao, R. Hauert, S. Tomizawa, T. Ishikawa, J. Ishi-Hayase, S. Shikata, C. L. Degen, and K. M. Itoh, Nano Lett. **13**, 4733 (2013).

[17] C. Osterkamp, J. Lang, J. Scharpf, C. Mller, L. P. McGuinness, T. Diemant, R. Behm, B. Naydenov, and F. Jelezko, Appl. Phys. Lett. **106**, 113109 (2015).

[18] J. F. Ziegler, J. P. Biersack, and M. D. Ziegler, *The Stopping and Range of Ions in Matter* (SRIM, Chester, MD, 2008).

[19] K. Nordlund, Comput. Mater. Sci. **3**, 448 (1995).

[20] G. Hobler, Radiat. Eff. Defects Solids **139**, 21 (1996).

[21] D. Antonov, T. Häußermann, A. Aird, J. Roth, H.-R. Trebin, C. Müller, L. McGuinness, F. Jelezko, T. Yamamoto, J. Isoya, S. Pezzagna, J. Meijer, and J. Wrachtup, Appl. Phys. Lett. **104**, 012105 (2014).

[22] J. Adler, A. Silverman, N. Ierushalmi, A. Sorkin, and R. Kalish, J. Phys.: Conf. Ser. **487**, 012015 (2014).

[23] A. Silverman, J. Adler, and R. Kalish, Phys. Rev. B **83**, 224206 (2011).

[24] K. Nordlund, M. Ghaly, R. S. Averback, M. Caturla, T. Diaz de la Rubia, and J. Tarus, Phys. Rev. B **57**, 7556 (1998).

[25] M. Ghaly, K. Nordlund, and R. S. Averback, Philos. Mag. A **79**, 795 (1999).

[26] J. Tersoff, Phys. Rev. Lett. **61**, 2879 (1988).

[27] K. Matsunaga, C. Fisher, and H. Matsubara, Jpn. J. Appl. Phys. **39**, L48 (2000).

[28] J. Tersoff, Phys. Rev. B **39**, 5566 (1989).

[29] E. H. Åhlgren, J. Kotakoski, and A. V. Krasheninnikov, Phys. Rev. B **83**, 115424 (2011).

[30] J. A. Golovchenko, D. E. Cox, and A. N. Goland, Phys. Rev. B **26**, 2335 (1982).

[31] See Supplemental Material at http://link.aps.org/supplemental/10.1103/PhysRevB.93.035202 for simulated depth profiles for Si ions with and without a graphitic contamination layer and displacement ranges of C atoms after implantation.

[32] P. K. Janert, *Gnuplot in Action* (Manning Publications, Shelter Island, NY, 2009).

[33] L. M. Pham, S. J. DeVience, F. Casola, I. Lovchinsky, A. O. Sushkov, E. Bersin, J. Lee, E. Urbach, P. Cappellaro, H. Park, A. Yacoby, M. Lukin, and R. L. Walsworth, arXiv:1508.04191.